Shahrood University of Technology

Journal of Mining and Environment (JME)

Journal homepage: www.jme.shahroodut.ac.ir

Iranian Society of Mining Engineering (IRSME)

Analytical and Numerical Stability Analysis of Underground Pillars Subjected to Shear Loading: A Case Study of the Chaabet El Hamra Zinc Mine, Algeria

Samia Chaoui[1], Adel Djellali[1*], Zied Benghazi[1], and Debojit Sarker[2]

1. Environmental Laboratory, Department of Mining and Geotechnology, Mining Institute, Echahid Cheikh Larbi Tebessi University, Tebessa, Algeria.
2. HNTB, 9 Entin Rd, Parsippany, New Jersey 07054, USA

Article Info

Received 16 August 2025
Received in Revised form 25 September 2025
Accepted 2 November 2025
Published online 2 November 2025

DOI: 10.22044/jme.2025.16677.3272

Keywords

Extraction rate
Inclined pillars
Safety factor
Analytical model
Numerical modeling

Abstract

This study aims to investigate the stability of rooms and pillars along the inclined zinc orebody at the Chaabet El Hamra underground mine (Setif, Algeria). Stability was initially assessed using an analytical shear strength model, with the results subsequently validated through numerical modeling. Geomechanical characterization revealed low interstitial porosity, strong to very strong uniaxial compressive strengths ranging from 50.4 MPa to 129 MPa, and significant fracture-related secondary porosity. Rock Mass Rating (RMR89) and Geological Strength Index (GSI) values suggest fair to good rock quality. The mine design features square pillars inclined at 10°, with walls originally oriented perpendicular to the orebody dip, measuring 5 m in width and 3 m in height. The rooms, situated under a cover depth of 145.3 m, are 9 m wide. This configuration yielded an effective extraction rate of 87.24% and a safety factor of 1.63, indicating stable mining conditions. Phase 2D finite-element simulation confirmed these findings, showing a maximum displacement of 3.96 mm, surface subsidence of 0.57 mm, and a safety factor of 1.66, suggesting minimal environmental impact and long-term stability. Shear/compressive stress results from tributary area theory, aligning with numerical results and validating both approaches for inclined orebodies. Finally, the pillar walls, originally perpendicular to the orebody dip, were modified to be vertical relative to the horizontal plane, while maintaining the same pillar and room dimensions and cover depth. This adjustment improved stability by enhancing stress distribution and pillar core confinement, increasing the safety factor to 1.85.

1. Introduction

The room-and-pillar mining method is typically chosen to extract sedimentary deposits, such as coal and zinc, especially in deposits that dip less than 30 degrees. It is used to leave pillars of intact material between mined openings, providing temporary or permanent support for the overburden [1, 2]. The objective is to recover as much ore as possible while allowing the mine as a whole to remain stable [3]. Since the loading environment at underground mines is complex, pillars can also experience different types of stress. Vertical pillars typically experience vertical compressive stress, while inclined pillars are subjected to a combination of compressive and shear stresses. These combined stresses change with the dip angle of the mineralized body [4, 5]. Once a pillar becomes unstable, it may cause the collapse of adjacent pillars, leading to roof falls and surface subsidence [6]. Pillar failure is more often related to the transition of compressive stresses into shear stresses rather than simply exceeding compressive strength [7]. Literature indicates that exposure to gases reduces the mechanical properties of coal pillars, such as shear strength and compressive strength, by generating fractures that can lead to unpredictable

Corresponding author: adel.djellali@univ-tebessa.dz

instabilities and outbursts underground [8, 9]. Sarfarazi et al. [10] and Fu et al. [11] demonstrated that both persistent and non-persistent joints, along with the choice of filling material, significantly affect the shear strength and failure mechanisms of jointed bedded rock masses. Consequently, evaluating pillar stability is essential for mine safety, and it requires extensive geological, geotechnical, and hydrogeological characterization of the orebody and surrounding rock masses to better understand the mechanical behavior and strength of the inclined pillars.

Several empirical equations [12-14] have been developed to estimate the strength of vertical hard rock pillars, taking into account an assumed width-to-height ratio and in situ compressive stress. Ghasemi et al. [15] implemented an artificial intelligence-based fuzzy system using the Mamdani algorithm to predict safe pillar dimensions in room-and-pillar coal mining, as analyzed in MATLAB, achieving R^2 values of 89.3% and 86.6% accuracy for pillar width and length, respectively. They identified loading conditions as the most important predictor. Ghasemi et al. [16] also developed predictive stability models based on the combination of logistic regression and fuzzy systems for global stability in retreat mining scenarios, and determined that pillar width was the most important variable affecting global stability. Kunkyin-Saadaari et al. [17] developed stacked generalization machine learning models to predict rock pillar stability at the Obuasi Gold Mine, with the Random Forest-stacked model yielding better accuracy. They identified pillar depth and stress as the primary environmental variables influencing stability. Abdollahi et al. [18] proposed a method based on the dynamic Coulmann Graphical technique for estimating side abutment load and chain pillar stability, which was implemented in the CCPSA software. This approach resulted in more consistent evaluations compared to the ALPS method or other traditional methods. Najafi et al. [19] utilized a Monte Carlo simulation combined with numerical modeling and empirical equations to assess the stability of chain pillars, finding that the failure probabilities were similar to those obtained using more sophisticated statistics. These results indicate that these advanced computational methods, when carefully applied, can lead to reliable stability predictions for column evaluation and design in mining engineering.

Although previous studies are mainly based on numerical simulation, in accordance with the objective of this study, special attention has been paid to both experimental tests and numerical simulations. Rezai et al. [20] examined gypsum samples with varying notch angle values under uniaxial loading conditions, finding that increasing the notch angle reduced both compressive strength and Young's modulus. Sarfarazi et al. [21] used a combination of experimental and numerical methods to assess the effect of the number and angle of joints on rock pillar failure. Their research showed that the strength of the specimens increased with the joint angle and the number of joints. Sarfarazi et al. [22] integrated experimental tests with 3D numerical simulations to examine the impact of various whole parameters (such as number, angle, and shape) on the load-bearing capacity and failure behavior of gypsum-simulated rock pillars subjected to uniaxial compression tests. Fu et al. [23] investigated the effects of axial loading width and immediate roof thickness on the failure mechanism and compressive strength of a notched roof in room-and-pillar mining, utilizing both experimental tests and numerical simulations.

While these methods primarily focus on vertical pillars, current research into inclined pillars mainly relies on laboratory compression-shear tests and numerical simulations. Jessu et al. [24] conducted compression-shear tests on gypsum and sandstone samples with diameters of 50 mm, but with various width-to-height ratios. Their results showed that pillar strength decreased as the inclination angle increased. He et al. [25, 26] performed combined compression-shear loading tests on basalt and granite samples, demonstrating that both the strength and elastic modulus of these rocks diminished with increasing sample inclination. As the angle of inclination increased, the failure mode of the rock samples transitioned from axial cracking to shear failure. Xu et al. [27] performed similar tests on samples of granite and confirmed that the failure strength exhibited a notable compression-shear coupling effect, and that the maximum failure strength decreased with larger inclination angles.

Numerical simulations that examined pillar strength at inclination angles of 0° to 40° concluded that shear failure was prevalent in inclined pillars and that the strength was strongly dependent on the inclination [28, 29]. Ma et al. [30] investigated the strength and failure modes of inclined pillars using a numerical model, and the authors found that the strength and failure modes depended on both the angle of inclination and the width-to-height ratio of the pillar. Garza Cruz et

al. [31] reported that shear stresses result in a considerable loss of confinement in pillar cores, thereby affecting load-bearing capacity and leading to strength loss [32]. According to Rashed et al. [33], combined compression and shear loads contribute to shear failure in inclined pillars. Das et al. [34, 35] investigated, via numerical modeling, the effect of geological layer inclination on the stability of the surrounding rock. They developed pillar models with various dip angles to analyze the influence of inclination on pillar strength, finding that the strength of an inclined pillar equates to that of a vertical pillar multiplied by a factor less than 1. Based on stress distribution characteristics and rock mass failure criteria, Das et al. [36] proposed a new strength formula able to calculate the resistance of both inclined and vertical pillars.

All the previous studies on inclined pillar strength clearly indicate that the inclination affects pillar strength due to the presence of shear stress. However, these investigations did not satisfactorily address the significant influence of shear stress on the load-bearing capacity of inclined pillars. Additionally, they often neglect how the orientation of pillar walls influences total pillar strength. An analytical shear strength model, defined by Sun et al. [37] and based on the Mohr-Coulomb failure criterion, was first presented to assess the strength and stability of inclined pillars under compression-shear loading conditions. This model was successfully utilized to evaluate both unstable and stable inclined coal pillars [35, 36], with results that corresponded to the observed behaviors. However, it has not yet been utilized in hard rock pillars, particularly those associated with zinc deposits.

The novelty of this work is in applying Sun et al.'s model to inclined zinc pillars in the lower part of the underground Chaabet El Hamra deposit at Ain Azel, Algeria. The validity of the model is evaluated via numerical simulation using Phase2D software. In addition, this study will also assess the effect of pillar wall orientation (the walls being either perpendicular to the roof of the inclined orebody, as is often required for stability, or vertical relative to the horizontal position) on pillar strength and stress distribution, to help improve as well as optimize mining operation performance and pillar stability.

2. General setting

2.1. Location of the study area

The Chaabet El Hamra zinc mine is located in the Chouf-Bouarket region, about 250 km southeast of Algiers and 50 km south of Setif. The mine's coordinates are 35°45' N latitude and 5°30' E longitude. It is located approximately 4.5 km from Ain-Azel and 12 km southeast of the Kherzet Youssef mining complex (Figure 1).

2.2. Geological conditions of the region

The Chaabet El Hamra deposit is located in the Hodna metallogenic zone, situated at the tectonic junction of three distinct geological structures: the Tell Atlas, the Saharan Atlas, and the High Plains (Figure 2). The structural formation of the deposit is influenced by folded structures and brittle faults. Its morphology features an anticline in the upper part and a monocline in the lower northwest part.

The lithostratigraphy of the deposit comprises several units (Figure 3), including the Valanginian unit, the Hauterivian unit, and the Barremian unit. The Valanginian unit, characterized by sterile deposits outcropping east of the eastern fault and west of the deposit, consists of alternating limestones, gray-green marls, sandstone, clay dolomites, and gray aleurolites with light gray quartzitic sandstones. Zinc mineralization is integrated into dolomites within the Lower Hauterivian. The Barremian unit, located to the south and northwest of the deposit, consists of alternating layers of sandstone, dolomites, marls, sandstones, and marly limestones.

2.3. Zinc mineralization

Zinc mineralization occurs within lenticular layers of massive or brecciated dolomite and is organized into two superimposed, stratiform, and subparallel orebodies. As shown in Figure 4, the section of profiles from 0 to 10 represents the upper part of the deposit, where the orebodies are horizontal and situated above the hydrostatic level (972 m) of a free water table. In contrast, the section of profiles from 10 to 15 represents the lower part of the deposit, where the orebodies are inclined at approximately 10°, extending northwest for about 500 m at depths ranging from 100 to 180 m below the hydrostatic level. The water table exists within the carbonate formations, which exhibit fractured permeability, including limestones and dolomites, while the substratum consists of marly formation. The two orebodies are separated by an interlayer of dolomite that is either poorly mineralized with zinc or sterile, with a thickness varying between 2 and 10 m. In some

cases, this interlayer is absent, resulting in the two orebodies merging into a single continuous body.

The average thicknesses of the lower and upper orebodies are approximately 4 m and 5 m, respectively. The roof of the upper orebody is composed of dolomite with marly beds, whereas the floor of the lower orebody consists of massive dolomite. To facilitate ore extraction, the National Company of Non-Ferrous Mining Products (ENOF) has installed a pumping system between profiles 15 and 16, which generates a cone of depression in the surrounding area of the mine [38].

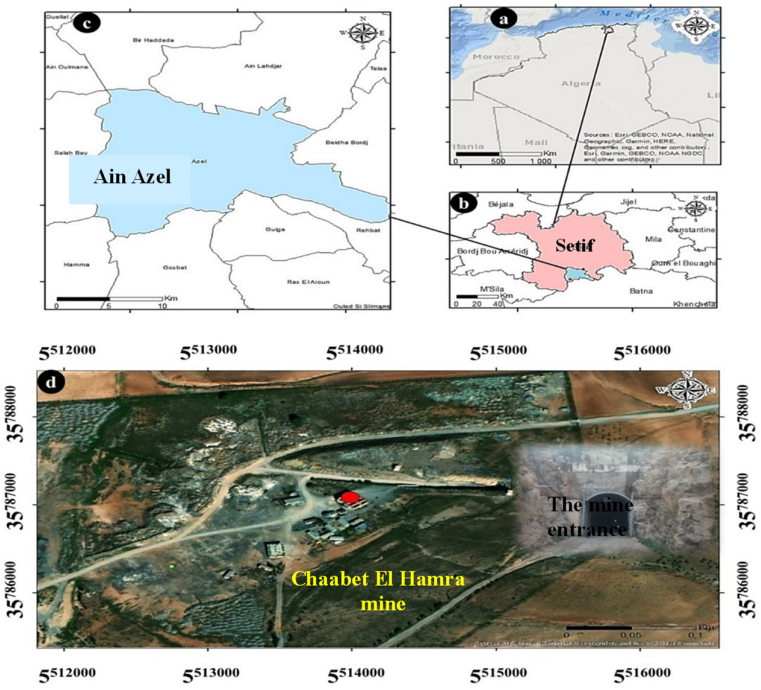

Figure 1. Geographical location of the study region

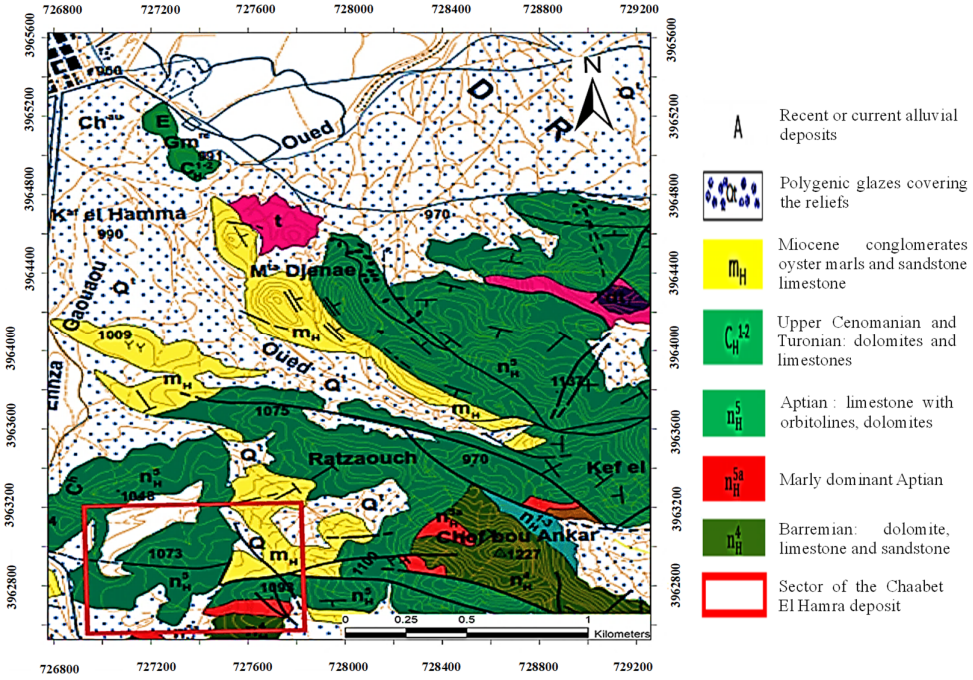

Figure 2. Geological map of the study area

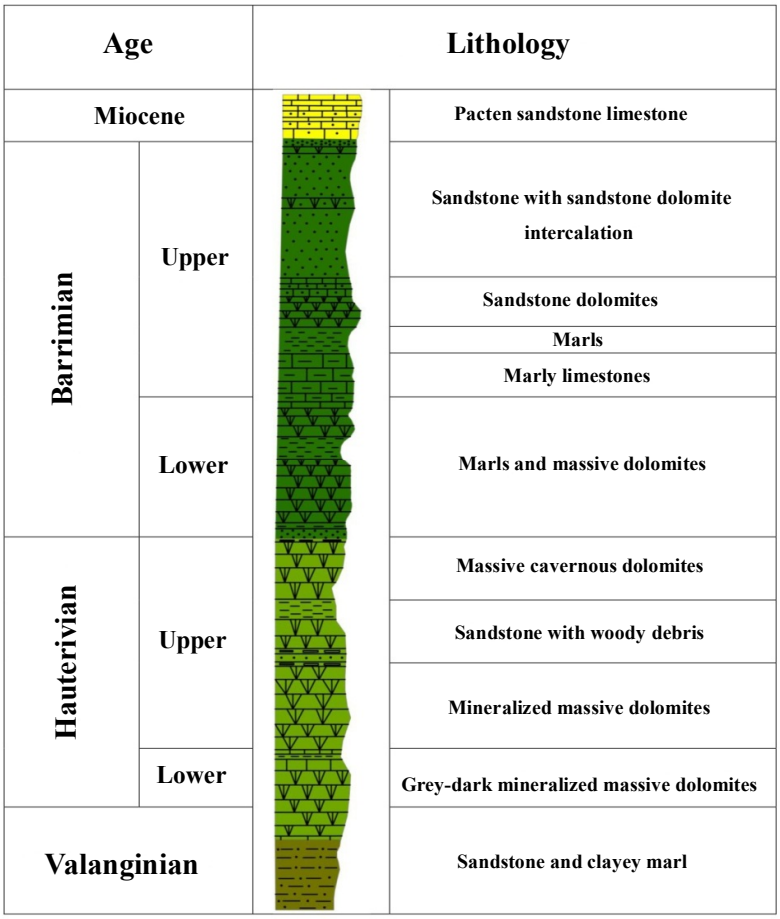

Figure 3. Lithostratigraphic column of the study area

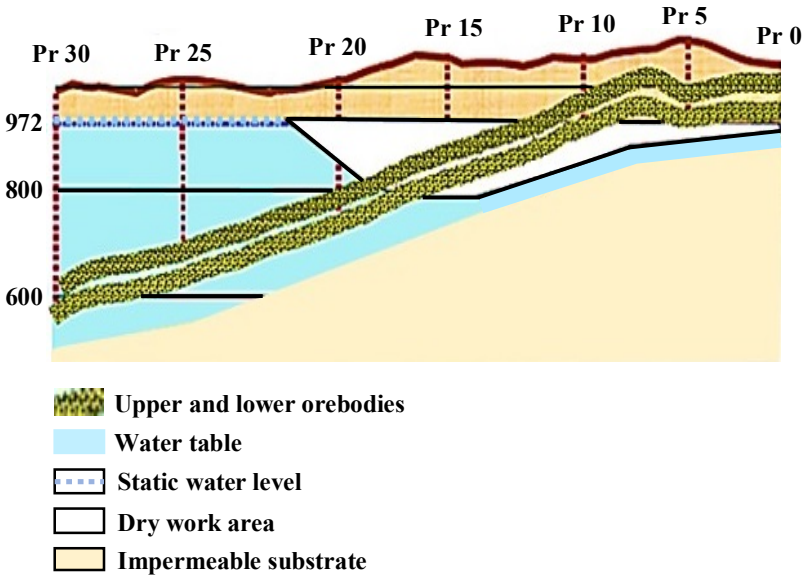

Figure 4. Geological cross-section showing the arrangement of the upper and lower orebodies relative to the static water table along the profile from Pr 0 to Pr 30

3. Materials and methods

3.1. Geotechnical characterization of the rock mass formations

This study focuses on the ore block located at profile 14. In this block, all rock strata (roof, orebody, and floor) are inclined at an angle of 10°. The ore consists of zinciferous dolomite with a thickness of 3.05 m. The overburden comprises nine superimposed geological formations with a total depth of 145.3 m, while the floor is composed of dolomite, as indicated in Table 1.

3.1.1. Laboratory testing of intact rock samples

Rock samples measuring 300 mm in length, 200 mm in width, and 150 mm in height were collected from different formations at the mine site and transported to the Mining, Metallurgy, and Materials Laboratory at the National Higher School of Technology and Engineering in Annaba for geotechnical characterization. Cylindrical specimens with a diameter of 54 mm were cored from these samples using a drilling machine. The core surfaces were then polished using a grinding machine to achieve a length-to-diameter ratio of between 2 and 2.5. For each lithology, 5 specimens were tested for uniaxial compressive strength, except for the organogenic sandstone, for which 8 specimens were tested (Figure 5), in accordance with the NF P94-420 [39] standard.

Additionally, 5 smaller cylindrical cores per lithology were prepared to assess physical properties, including wet density, dry density, saturated density, and porosity. Dry density measurements were conducted after the samples were oven-dried at 105°C for 24 hours, following the guidelines in NF P94-064 [40].

Table 1. Geometric characteristics of the rock mass layers

Lithology	Zone	Dip (°)	Thickness (m)
Sandstone limestone	Roof	10	12
Low sandstone and porous dolomite	Roof	10	28
Marly limestone oxidized in places	Roof	10	17
Sandstone dolomite	Roof	10	18
Lilac sandstone	Roof	10	6.4
Hematitized dolomite with calcite veins	Roof	10	20.1
Compact clayey and sandstone dolomite	Roof	10	23.1
Organogenic sandstone	Roof	10	4.4
Dolomite	Roof	10	16.3
Zinciferous dolomite	Orebody	10	3.05

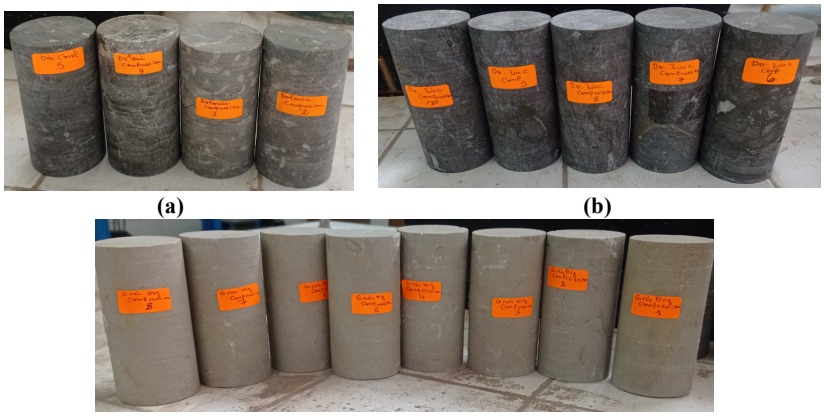

Figure 5. Intact rock specimens prepared for uniaxial compression testing: (a) dolomite, (b) zinciferous dolomite, and (c) organogenic sandstone

3.1.2. Discontinuities

During fieldwork, 200 measurements of natural discontinuities (dip direction and dip angle) were collected along the walls of the galleries using a geological compass and field notebook. These joints were grouped into major families based on their orientations using GeoRose v.0.5.2 software. For each joint set, key characteristics, i.e., aperture, weathering, roughness, and infill material, were documented. These parameters were subsequently incorporated into empirical formulas for rock mass quality

classification, such as the Rock Mass Rating System (RMR_{89}) [41].

3.1.3. Rock mass rating (RMR_{89}) and geological strength index (GSI)

In rock engineering projects, the RMR and GSI classification systems are commonly used to improve the reliability of rock mass quality assessment. The RMR_{89} provides a detailed classification based on several quantitative parameters such as uniaxial compressive strength (UCS), rock quality designation (RQD), and hydrogeological conditions. Nevertheless, the GSI relies on qualitative observations of the rock mass structure and the surface condition of discontinuities, allowing for the estimation of rock mass strength and deformability parameters. The complementary use of both systems allows for cross-validation of results, ensuring a more accurate and robust characterization of rock mass behavior under various geological conditions. This combined approach is essential for the design of underground structures and numerical modeling, ensuring better consideration of site-specific geological and geotechnical specificities.

The RMR system evaluates rock mass quality using six parameters, assessed in this study as follows:

- Uniaxial compressive strength (UCS): Measured in the laboratory from representative samples of intact rock;
- Rock quality designation (RQD): Estimated from core logging data collected from the geotechnical subsurface exploration;
- Spacing of discontinuities (Js): Measured directly from gallery wall surveys in the ore layer, and estimated using geotechnical data for the overburden rock layers;
- Condition of discontinuities (Jc): Assessed through field observation of joint weathering, infill material, and surface roughness;
- Groundwater conditions (Jw): Evaluated using hydrogeological data;
- Orientation of discontinuities (Jo): Analyzed in relation to the direction of excavation.

Each parameter is assigned a numerical rating, and the overall RMR value is calculated by summing these ratings [42]. The rock mass quality is then categorized based on the RMR value, as detailed in Table 2.

In this study, the GSI was estimated using the chart developed by Hoek and Marinos [43]. This estimation is based on field observations of the rock mass structure, as well as the surface conditions of the discontinuities, including attributes such as roughness, weathering, and infill.

Table 2. Classification of rock mass quality based on RMR values

RMR range	Rock mass quality
81 to 100	Very good
61 to 80	Good
41 to 60	Fair
21 to 40	Poor
20 or below	Very poor

3.1.4. Rock mass properties

The strength and deformation properties of rock masses were evaluated based on the equations proposed by Hoek et al. [44]. These parameters were estimated by adjusting intact rock parameters using two key factors: the geological strength index (GSI) and the disturbance factor (D). The generalized Hoek-Brown criterion for jointed rock masses is:

$$\sigma_1' = \sigma_3' + \sigma_{ci}\left(m_b \frac{\sigma_3'}{\sigma_{ci}} + s\right)^a \quad (1)$$

where σ'_1 and σ'_3 are the major and minor effective principal stresses at failure, σ_{ci} is the uniaxial compressive strength of intact rock, and m_b, s, and a are empirical constants dependent on the intact rock constant m_i, GSI, and disturbance factor D (ranging from 0 for undisturbed to 1 for disturbed rock mass).

Once the failure criterion is established, additional rock mass properties are determined using the RocLab 1.0 program and the Hoek-Brown method [44]. The main evaluated properties include the tensile strength (σ_t), compressive strength (σ'_{cm}), deformation modulus (E_m), friction angle (φ), and cohesion (c).

The Poisson's ratio for the rock mass (ν_m) can be estimated using the following relationship [45]:

$$\nu_m = 0.25\left(1 + e^{-\sigma'_{cm}/4}\right) \quad (2)$$

3.2. Analytical evaluation of pillar stability in inclined orebodies

Following the geomechanical characterization of the rock formations, square-shaped inclined pillars measuring 3 m in height and 5 m in width were selected, along with inclined rooms 9 m wide, at an overburden depth of 145.3 m. Compressive and shear stresses acting on the pillars were initially calculated using the tributary area method. Subsequently, the stability of the

pillars was evaluated using the analytical shear strength model proposed by Sun et al. [37], originally formulated for coal and hard rock pillars. However, this model was not validated only in a limited number of coal mines, nor was it applied to hard rock settings.

In this study, a novel application of Sun et al. model [37] was disseminated to the Chaabet El Hamra zinc ore deposit, which is characterized by hard rock lithologies. Simultaneously, the reliability of the analytical solutions was validated by comparing them with those obtained from numerical simulations that incorporate site-specific geotechnical parameters.

3.2.1. Stress calculation of the inclined pillar using the tributary area theory

The tributary area method, typically used for regularly arranged vertical pillars of similar sizes, assumes each pillar supports its direct overhead load plus half the load from adjacent rooms. For inclined orebodies, pillar stress is adjusted according to the orebody's dip angle (Figure 6) [46]. The average normal compressive stress (σ_n) and shear stress (τ) on inclined pillars are:

$$\sigma_n = \gamma H \frac{1}{1 - R} (cos^2 \theta + K \ sin^2 \theta) \quad (3)$$

$$\tau = \gamma H \frac{1}{1 - R} cos\theta \ sin\theta \ |(1 - K)| \quad (4)$$

Where θ is the orebody dip angle in degrees, H is the average orebody buried depth in meters, γ is the average overburden wet unit weight in MN/m^3, K is the horizontal to vertical in situ stress ratio, and R is the extraction ratio defined as the ratio of mined area to total area.

For square pillars, the extraction ratio R is given by:

$$R = \frac{(w + B)^2 - w^2}{(w + B)^2} \quad (5)$$

Where w is the pillar width, and B is the room width, both measured in meters.

K is calculated as:

$$K = \frac{\nu_m}{1 - \nu_m} \quad (6)$$

Where ν_m is the Poisson's ratio of the rock mass.

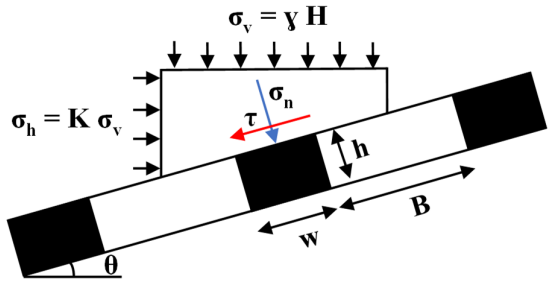

Figure 6. Stresses acting on the inclined pillar

3.2.2. Shear strength model

Sun et al. [37] proposed a shear strength model to assess the bearing capacity of an inclined pillar subjected to combined compression and shear loads. This model is based on the Mohr-Coulomb theory and relies on the strength of a vertical pillar (S_{p0}) as well as a shear load contribution factor (F).

Several key points are identified and illustrated in Figure 7, which relates the Mohr-Coulomb strength envelope to Mohr's stress circle. The radius of the maximum stress circle for the vertical pillar is given by:

$$OA = AB = O.5 \ S_{p0} \quad (7)$$

The radius of the maximum stress circle for the inclined pillar is given by:

$$OC = CD = CF + FD = CF + GB \quad (8)$$

Where Point B represents the tangent point where the strength envelope intersects the maximum stress circle of the vertical pillar, and Point D represents the tangent point for the inclined pillar.

$$\begin{cases} CF = OC \ sin \ (\varphi - \beta) = \dfrac{EC}{sin\,\beta} \ sin \ (\varphi - \beta) = \dfrac{0.5\,\tau}{sin\,\beta} \ sin \ (\varphi - \beta) \\ GB = AB - AG = 0.5 \ S_{p0} \ (1 - sin \ \varphi) \end{cases} \quad (9)$$

Where Point E is the intersection of the vertical line passing through point C with the σ-axis.

By substituting equation (9) into equation (8), we obtain:

$$\tau = \frac{(1 - sin \ \varphi) \ sin \ \beta}{1 - sin(\varphi - \beta)} \times S_{p0} \quad (10)$$

Equation (10) represents the limit equilibrium condition for shear stress on the inclined pillar, where the left side denotes the shear stress acting on the pillar, and the right side represents the shear strength (S_p). If the shear stress exceeds the shear strength (i.e., if the right side is smaller than the left), this indicates that the pillar is likely to fail.

The inclined pillar is characterized by the presence of shear load compared to the vertical pillar. The contribution factor of shear load (CFSL), denoted by the symbol F, is determined by the ratio of the shear strength (S_p) of the inclined pillar to the compressive strength (S_{p0}) of the vertical pillar. An increase in the CFSL value results in a reduction of the pillar's bearing capacity.

$$F = \frac{S_p}{S_{p0}} = \frac{(1 - \sin\varphi)\ \sin\beta}{1 - \sin(\varphi - \beta)} \quad (11)$$

Where: φ is the friction angle of the ore, and β is the dip of a straight line passing through the center of the stress circle, corresponding to the equivalent internal friction angle of the inclined pillar:

$$\tan\beta = \frac{\tau}{\sigma_n} = \frac{(1 - K)\ \sin(2\theta)}{(1 + K) + (1 - K)\ \cos(2\theta)} \quad (12)$$

The safety factor (Sf) of the inclined pillar is defined as the ratio between shear strength (S_p) and shear load (τ):

$$Sf = \frac{S_p}{\tau} = \frac{F \times S_{p0}}{\gamma H \dfrac{\sin\theta\ \cos\theta\ (1 - K)}{1 - R}} \quad (13)$$

The pillar is considered stable when Sf ≥ 1.5 [36, 47]

It is essential to select the most appropriate empirical formula to estimate the strength of vertical pillar (S_{p0}). For the purpose of this study, the correlation proposed by Lunder and Pakalnis [14] was selected, as it is derived from a database of massive sulfide rock masses containing valuable metals such as zinc and lead. This formula is based on the confinement parameter and is expressed as follows:

$$S_{p0} = 0.44\ \sigma_{ci}\ (0.68 + 0.52\ \text{ƙ}) \quad (14)$$

Where 0.68 and 0.52 are empirical rock mass constants, σ_{ci} is the uniaxial compressive strength of the intact rock in MPa, 0.44 is the pillar size factor, and ƙ is the pillar friction term, determined by:

$$\text{K} = \tan\left[\cos^{-1}\left(\frac{1 - C_{pav}}{1 + C_{pav}}\right)\right] \quad (15)$$

$$C_{pav} = 0.46 \times \left[\log\left(\frac{w}{h} + 0{,}75\right)\right]^{\frac{1.4}{(w/h)}} \quad (16)$$

Where C_{pav} is the average pillar confinement, and w/h is the width-to-height ratio of the pillar.

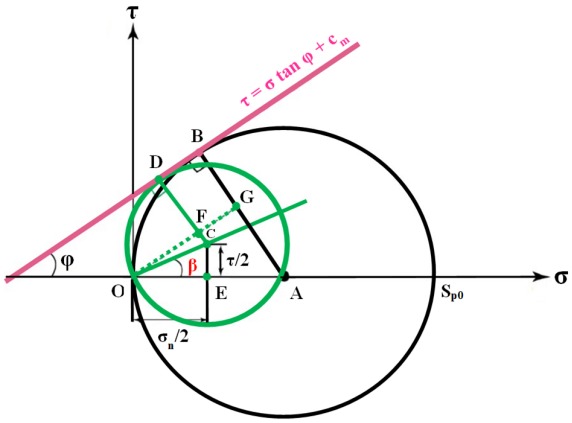

Figure 7. The relationship between Mohr's stress circle and Mohr-Coulomb strength envelope [37]

4. Results and discussions

4.1. Geotechnical characterization

4.1.1. Lab test results

Table 3 presents the physical and mechanical properties of intact rocks from various formations.

Table 3. The physicomechanical properties of intact rocks (roof, orebody, and floor)

Lithology	γ_d (kN/m³)	γ_h (kN/m³)	γ_{sat} (kN/m³)	p (%)	σ_{cmin} (MPa)	σ_{cmax} (MPa)	σ_{cmean} (MPa)
Sandstone limestone	27.1	27.2	27.5	3.97	54.6	56.72	55.42
Low sandstone and porous dolomite	26.2	26.5	27.3	11.34	49	51.8	50.4
Marly limestone oxidized in places	27.4	27.6	28.9	15.10	79.5	84	82.6
Sandstone dolomite	27.6	27.9	28.1	4.98	127.9	130	129
Lilac sandstone	25.3	25.8	26.3	9.53	105	110	108
Hematitized dolomite with calcite veins	27.8	28.2	28.4	6.35	79.9	85	80.9
Compact clayey and sandstone dolomite	28.5	28.7	28.8	3.48	89	92.4	90.5
Organogenic sandstone	26.4	26.6	27.2	7.30	102.45	104.6	103.57
Dolomite	27.9	28	28	1.46	79.9	83.95	82.93
Zinciferous dolomite	30.6	30.7	30.7	2.13	115.8	120.4	118.75

Based on the results presented in Table 3, the average compressive strength values reported for each rock type are considered representative, given the small difference between the minimum and maximum compressive strength (σ_{cmin} and σ_{cmax}) measurements. This limited variability indicates a consistent mechanical behavior across the tested samples. Such homogeneity can be attributed to the geological continuity and uniform lithological properties within each layer, as supported by both field observations and geological studies.

According to the French Tunneling and Underground Space Association (AFTES) [48], all rocks from different formations are categorized as having strong to very strong compressive strength (ranging from 50.4 MPa to 129 MPa) and low to moderate porosity (ranging from 1.46% to 15.10%). The relatively low porosity values indicate that these formations are composed of dense, massive, and compact rocks with limited internal void space, contributing to their overall strength and stability.

Despite the relatively low interstitial porosity (ranging from 1.46% to 15.10%), the presence of the groundwater table suggests that these formations may exhibit permeability due to secondary porosity, which arises from fractures that allow water to flow through the rock [49]. The elevated strength values are primarily attributed to the low porosity and compact nature of the rocks [50].

4.1.2. Discontinuities

A structural analysis conducted using GeoRose v.0.5.2 software reveals that the rock mass is highly fractured, featuring four predominant joint sets (Figure 8) that are randomly oriented and uniformly distributed, resulting in an approximately isotropic mechanical behavior. These joint sets are characterized as follows: Set 1 (NNE-SSW) strikes between N15° and N20° with a dip angle of 70°; Set 2 (NE-SW) strikes between N40° and N55° with a dip angle of 82°; Set 3 (ENE-WSW) strikes between N80° and N85° with a dip angle of 76°; and Set 4 (ESE-WNW) strikes between N110° and N120° with a dip angle of 68°. The joints exhibit slightly rough and weathered surfaces, with apertures ranging from 1 to 5 mm, and are typically filled with calcite, quartz, and iron oxide minerals.

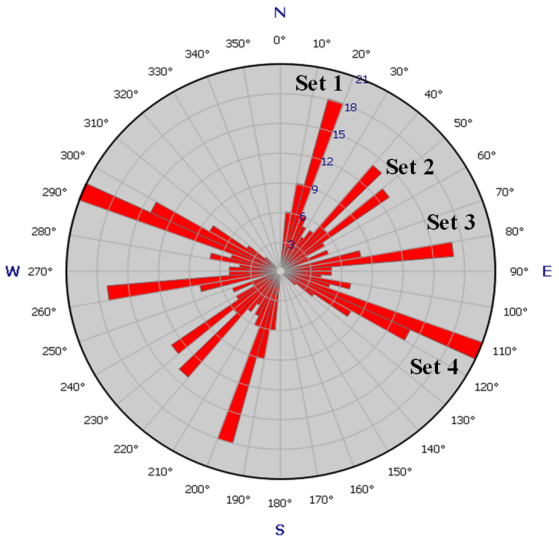

Figure 8. Rose diagram showing the joint directions of the analyzed joint sets

4.1.3. RMR_{89}

Table 4 presents the results of the RMR_{89} classification system for the rock mass formations based on field observations and laboratory data.

Table 4. RMR Classification results for the rock mass lithologies

Lithology	RQD (%)	UCS	RQD	Js	Jc	Jw	Jo	RMR_{89}
Sandstone limestone	63	7	13	10	15	10	-5	50
Low sandstone and porous dolomite	70	7	13	10	17	10	-5	52
Marly limestone oxidized in places	75	7	13	10	15	10	-5	50
Sandstone dolomite	69	12	13	10	17	10	-5	57
Lilac sandstone	75	12	13	10	15	10	-5	55
Hematitized dolomite with calcite veins	54	7	13	10	15	10	-5	50
Compact clayey and sandstone dolomite	51	7	13	10	17	10	-5	52
Organogenic sandstone	70	12	13	10	17	10	-5	57
Dolomite	70	7	13	10	17	10	-5	52
Zinciferous dolomite	75	12	13	10	17	10	-5	57

Legend: UCS: uniaxial compressive strength; RQD: rock quality designation; Js: joint spacing; Jc: joint conditions; Jw: hydraulic joint conditions; Jo: joint orientation; RMR89: rock mass rating.

The results presented in Table 4 provide a detailed assessment of the studied rock formations based on Bieniawski's method [42]. The main observations are as follows:

All rock formations received a rating of 7 for the UCS parameter due to their high strength values (ranging from 50.4 MPa to 90.5 MPa), except for sandstone dolomite, lilac sandstone, organogenic sandstone, and zinciferous dolomite, which received a high rating of 12 due to their very high strength values (ranging from 103.57 MPa to 129 MPa). All rock formations were assigned an RQD rating of 13, indicating fair quality (between 51% and 75%). For joint spacing (Js), all formations were rated 10, indicating that the discontinuities are moderately spaced (between 200 and 600 mm). Regarding the joint conditions (Jc) parameter, all formations received a rating of 17, indicating that the joints are slightly weathered and rough, with openings ranging from 1 to 5 mm and filled with hard materials such as calcite and iron oxide. Exceptions include sandstone limestone, marly limestone, lilac sandstone, and hematitized dolomite, which received a rating of 15 due to increased weathering. For joint orientation (Jo), all formations received a value of -5, indicating that the orientation of the joints relative to the direction of mining operations is fair. All formations were rated 10 for the groundwater (Jw) parameter, indicating a damp state.

Therefore, the RMR values suggest that all analyzed lithologies fall within the fair quality range (between 50 and 57), indicating relatively stable geotechnical conditions with inherent risks during mining operations.

4.1.4. GSI

Figure 9 illustrates a chart used to determine the GSI values for the rock mass formations. The GSI values indicate that the rock mass lithologies ranges from fair to good quality, falling between 53 and 60, with a blocky to very blocky structure. This classification is consistent with the RMR system in terms of rock quality assessment. Within this GSI range, the rock mass is considered moderately competent, exhibiting an overall intact and stable structure, though it includes various fractures and discontinuities that affect its mechanical behavior. These structural features are crucial in controlling the rock mass's response under stress, especially regarding failure mechanisms. In this study, failure is primarily influenced by a combination of compressive and shear stresses acting on the inclined pillars. The anticipated failure mode involves shear failure initiating at two diagonally opposite corners of the highly stressed inclined pillar and propagating inward toward its core.

4.1.5. Rock mass properties

Table 5 presents the Mohr-Coulomb strength and deformation parameters for the rock layers derived from the generalized Hoek-Brown criterion. These parameters were determined using different disturbance factors based on site observations, including the presence of discontinuities, joint conditions, and the impact of blasting. Specifically, a disturbance factor of D = 0.7 was applied to the zinciferous dolomite ore, and D = 0.5 for the dolomite, reflecting localized damage caused by uncontrolled blasting and pre-existing fractures within the rock mass. For other rock types located above and away from excavation zones, a disturbance factor of D = 0 was assigned, considering their limited exposure to such disturbances.

4.2. Analytical analysis results

Table 6 presents the stability analysis outcomes for the proposed inclined rooms and pillars, based on the analytical shear strength model. The design, which incorporates pillars 5 m wide and rooms 9 m wide, achieves an extraction rate of 87.24% with a safety factor of 1.63. These results indicate a stable and secure mining operation with efficient ore recovery.

Table 5. m_i values and Mohr-Coulomb parameters for the rock mass lithologies

Lithology	m_i	D	c (MPa)	φ (°)	σ_t (Mpa)	E_m (MPa)	ν_m
Sandstone limestone	8	0	0.92	45.29	0.20	8848	0.27
Low sandstone and porous dolomite	7	0	0.91	44.06	0.24	9467	0.28
Marly limestone oxidized in places	10	0	1.26	50.36	0.28	12120	0.25
Sandstone dolomite	11	0	2.08	54.73	0.58	17783	0.25
Lilac sandstone	15	0	1.72	56.80	0.35	17783	0.25
Hematitized dolomite with calcite veins	9	0	1.25	49.14	0.30	11994	0.26
Compact clayey and sandstone dolomite	9	0	1.36	49.76	0.34	12686	0.25
Organogenic sandstone	15	0	1.69	56.39	0.34	17783	0.25
Dolomite	9	0.5	1.11	46.75	0.27	11466	0.26
Zinciferous dolomite	11	0.7	1.29	48.48	0.30	11559	0.25

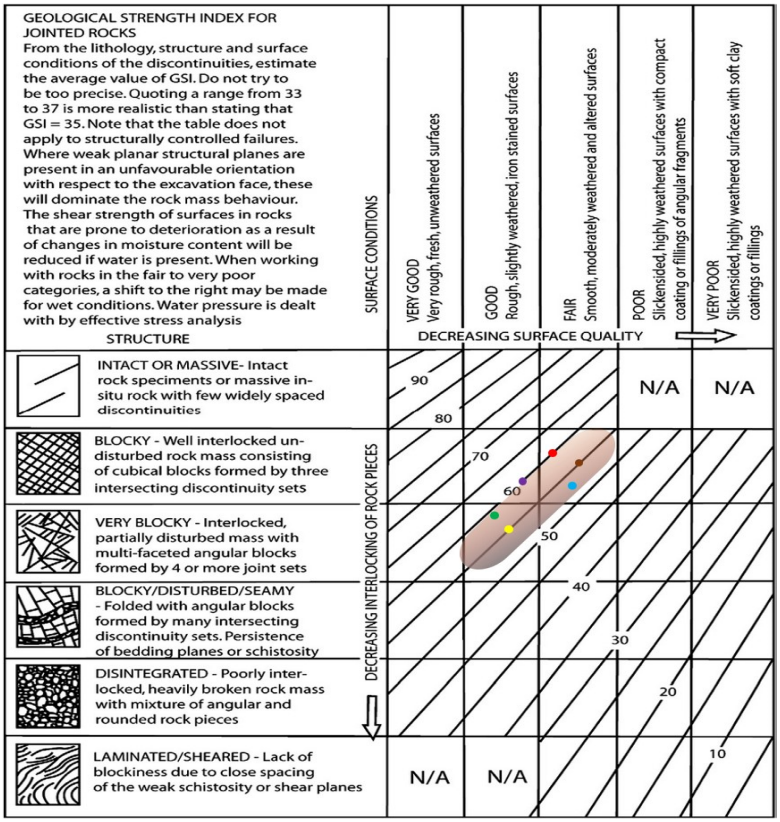

Figure 9. Chart for estimating the GSI of jointed rock masses [43]

Table 6. Stability parameters of the proposed inclined pillars

Parameters	θ (°)	H (m)	ɣ (kN/m³)	φ (°)	σ_c (MPa)	K	h (m)	w (m)	B (m)	R (%)	S_{p0} (MPa)	S_p (MPa)	β (°)	Sf
Values	10	145.3	27.6	48.48	118.75	0.33	3	5	9	87.24	67.05	5.87	6.67	1.63

θ: orebody dip angle; H: average orebody buried depth; ɣ: average wet unit weight of the overburden; φ: internal friction angle of the orebody; σ_c: uniaxial compressive strength of the intact rock; K: in situ stress ratio; h: pillar height; w: pillar width; B: room width; R: ore extraction rate; S_{p0}: compressive strength of the vertical pillar; S_p: shear strength of the inclined pillar; β: equivalent internal friction angle of the inclined pillar; Sf: safety factor of the inclined pillar.

4.3. Numerical modeling results

While the analytical approach provides a robust foundation for pillar design, numerical modeling using the finite element method (FEM) has been employed to validate this approach under more realistic geotechnical conditions. FEM enables the precise and detailed simulation of the complex behavior of inclined pillars by accounting for rock mass heterogeneity, material nonlinearity, interactions between pillars and the surrounding rock, interactions among multiple pillars, and boundary effects. It also allows for thorough evaluation of stress and strain distribution, quantification of surface subsidence, and analysis of potential failure modes. By combining analytical and numerical approaches, results can be cross-validated, leading to a more comprehensive and reliable assessment of the geomechanical behavior and long-term stability of the room-and-pillar system.

4.3.1. Model development and geometry

The Phase 2D Finite Element program was used to create two numerical models of 10° inclined pillars. The first model contains five pillars with ribs perpendicular to the orebody floor (A-pillars) (Figure 10(a)), while the second model consists of five pillars with vertically oriented ribs (B-pillars) (Figure 10(c)). Both models maintain a 5 m pillar width and a 9 m room width at an average depth of 145.3 m. The first model is intended to validate the analytical stability results, while the second is designed to assess the influence of pillar rib orientation on principal stress distribution, displacement, and safety factor. Following Lorig and Cabrera's recommendation [29], five pillars were modeled instead of a single pillar to better represent multiple-pillar behavior in inclined orebodies.

Roller boundary conditions were applied at a sufficient distance from rooms and pillars, particularly far from the central pillar, to minimize boundary effects and errors in the results. To stabilize the numerical models and realistically simulate the stress distribution in the rock mass, surface displacements were left unconstrained, while vertical and horizontal restraints were applied to the sides and bottom of the models. The model comprises three geotechnical units: the overburden (consisting of nine rock formations), the orebody, and the dolomitic roof. The mechanical behavior of these units was described using the Mohr-Coulomb model, which allows for the assessment of stress distribution and the stability of inclined pillars based on elastic parameters (Young's modulus and Poisson's ratio) and perfectly plastic parameters (cohesion, friction angle, and tensile strength), as detailed in Table 5. An in-situ stress ratio (K) of 0.33 and an average wet unit weight of 27.6 kN/m^3 for the overburden were used. Both models utilized a graded 3-node triangular mesh (gradation factor 0.1) and refined elements with a size of 0.42 meters for the pillars to ensure accurate results, totaling approximately 16,000 elements and 8,000 nodes.

The analysis was conducted in two stages: (1) pre-mining in situ stress initialization and (2) room excavation phase.

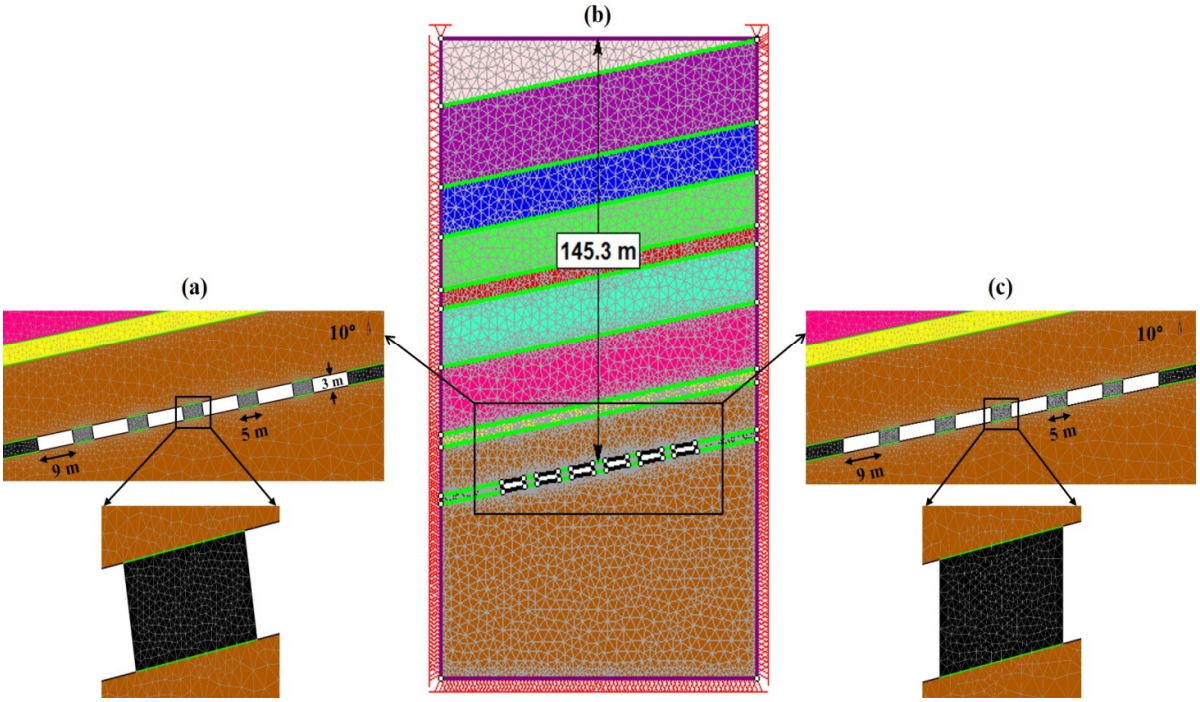

Figure 10. Models of 10° inclined pillars: (a) ribs oriented perpendicular to the floor (A-pillars), (b) complete mesh generation showing refined discretization near pillars and rooms, (c) ribs positioned vertically (B-pillars)

4.3.2. Maximum and minimum stress distributions

Figure 11 illustrates the distributions of maximum principal stresses and confining stresses for the inclined central A-pillar and B-pillar. For the inclined central A-pillar (ribs oriented perpendicular to the floor) in Figure 11(a), the maximum principal stress distribution is

asymmetrical, concentrating in two diagonally opposite corners: the upper right corner at the roof and the lower left corner at the floor. In these regions, the maximum principal stresses reach high values of 21.51 MPa and 22.29 MPa, respectively; however, failure in this zone is not considered critical. In contrast, the inclined central B-pillar (ribs positioned vertically) (Figure 11(b)) shows relatively symmetrical and uniform maximum principal stress distribution across all four corners. The stresses at the upper right corner (roof) and lower left corner (floor) decrease to 18.20 MPa and 18.49 MPa, respectively. This symmetrical distribution suggests that vertical wall geometry is more compatible with orebody inclination, leading to enhanced stability compared to perpendicular-walled pillars.

Furthermore, this symmetrical stress distribution contributes to higher core confinement in the central B-pillar, measuring 2.69 MPa (Figure 11(d)), compared to 2.39 MPa in the central A-pillar (Figure 11(c)). This increased confinement enhances the long-term bearing capacity of inclined pillars with vertical walls, thereby reducing the risk of failure.

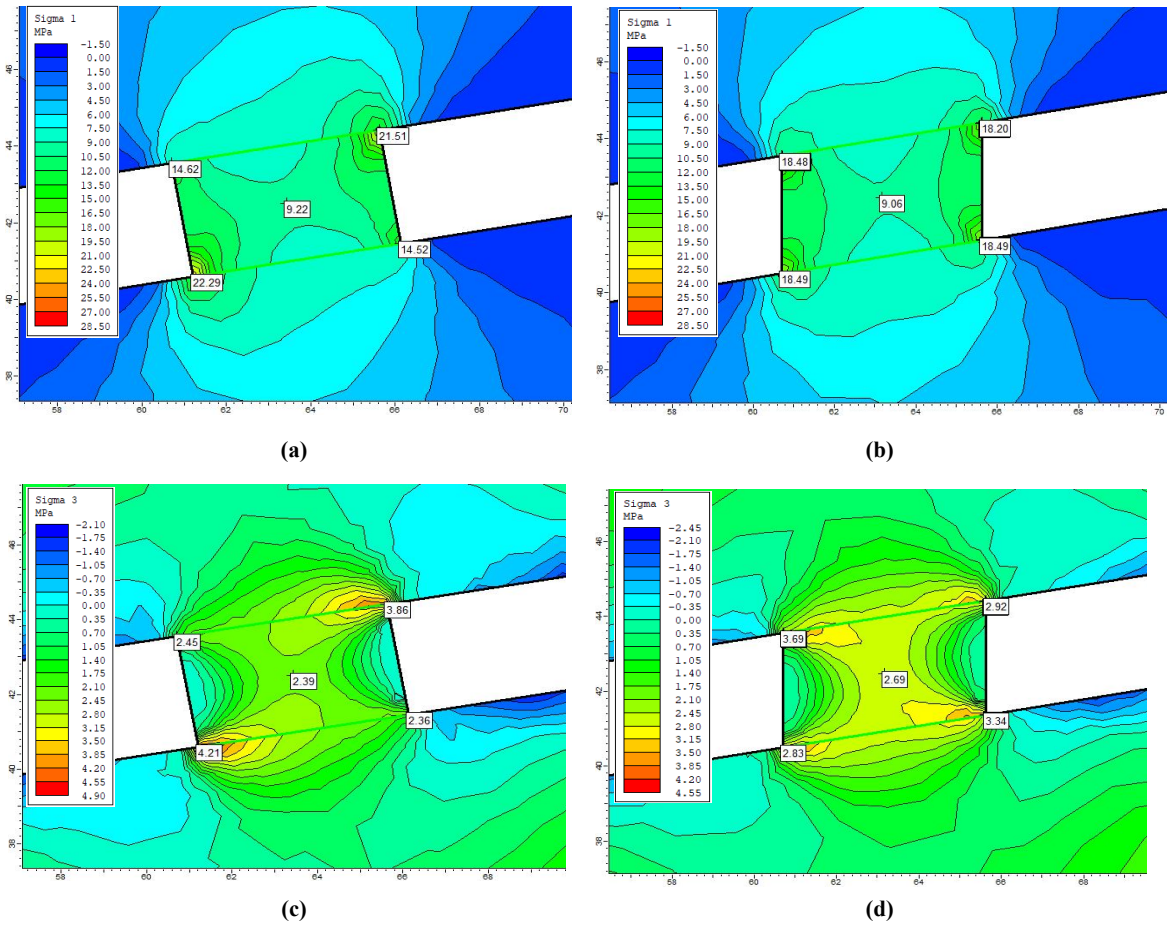

Figure 11. Contour lines of principal stress distributions in inclined central pillars: (a) and (c) maximum and minimum principal stresses, respectively, in inclined A-pillar; (b) and (d) maximum and minimum principal stresses, respectively, in inclined B-pillar

The results presented in Figure 12 confirm and validate the major principal stress distribution patterns observed in Figure 11 for both pillar configurations. For the 10° A-pillar (Figure 12(a)), the graph highlights the asymmetrical stress concentration along the diagonals, creating localized high-stress zones in the upper right corner of the roof and the lower left corner of the floor. These stress peaks increase the likelihood of failure initiation in these areas of the pillar as they approach or locally exceed the pillar's strength, potentially leading to the formation of fractures. This localized overstressing compromises the structural integrity of the pillar over the long term. In contrast, the 10° B-pillar (Figure 12(b)) exhibits a more uniform stress distribution pattern.

This uniformity suggests a lower risk of localized failure, as the stresses are evenly distributed throughout the pillar, avoiding localized stress concentrations. This contributes to the overall stability and safety of the pillar, making it a more favorable configuration for inclined orebodies.

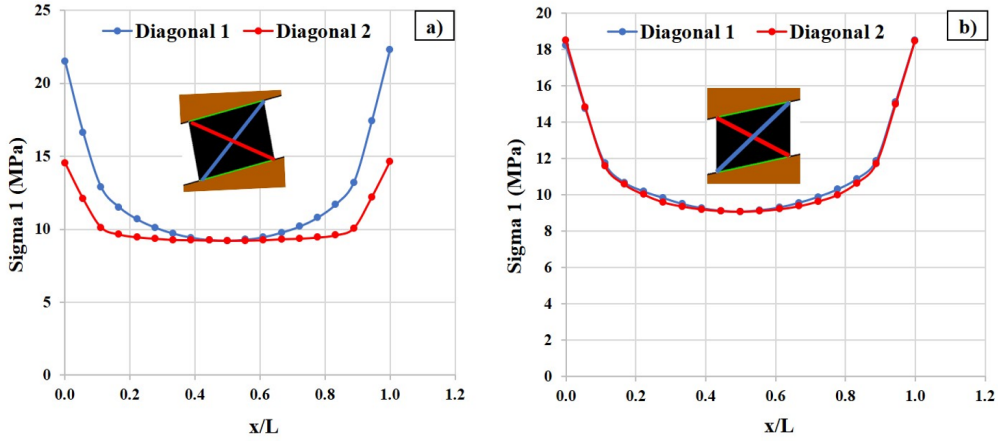

x: distance from the first point (m) and **L**: length of diagonal 1 or diagonal 2 (m).

Figure 12. Variation of the major principal stress along the two diagonals of the inclined central pillar: (a) 10° A-pillar; (b) 10° B-pillar

4.3.3. Normal and shear stresses

Table 7 summarizes the results of pre-mining normal and shear stresses in the inclined central pillar, calculated using both the tributary area method (equations 13 and 14) and the numerical modeling technique. The findings reveal that the pre-mining normal (σ_0) and shear (τ_0) stresses obtained from both methods are identical at 3.93 MPa and 0.46 MPa, respectively. This perfect agreement validates the reliability and effectiveness of both approaches in evaluating the stress conditions within the inclined pillar.

4.3.4. Total displacements

The total displacement analysis, illustrated in Figure 13, reveals similar patterns for both pillar configurations, with maximum displacements occurring at the center of the central chamber roofs. The rooms supported by perpendicular-walled pillars (A-pillars) show a maximum displacement of 3.96 mm (Figure 13(a)), while those supported by vertical-walled pillars (B-pillars) exhibit a slightly lower displacement of 3.89 mm (Figure 13(b)). These values are well within acceptable limits according to previous studies [51, 52] despite being subject to both normal compressive stress from overburden weight and tangential shear stress induced by inclined layering. Surface displacement measurements further confirm the stability of both configurations, with notably small values of 0.57 mm and 0.55 mm for inclined A-pillars and B-pillars, respectively. These minimal surface displacements indicate negligible subsidence risk and validate the overall structural stability of both pillar arrangements.

Table 7. Comparison of pre-mining normal and shear stresses in the inclined central pillar

Stress analysis method	σ_0 (MPa)	τ_0 (MPa)
Tributary area theory	3.93	0.46
Phase 2D	3.93	0.46

4.3.5. Safety factor

According to Figure 14, the safety factor analysis demonstrates stability for both pillar configurations. The inclined pillars with walls perpendicular to the floor (Figure 14(a)) show a central pillar safety factor of 1.66, which validates the analytically calculated value of 1.63. For pillars with vertical walls (Figure 14(b)), the safety factor increases to 1.85 for the central pillar, resulting from the higher confinement at the pillar's core, which enhances its strength capacity.

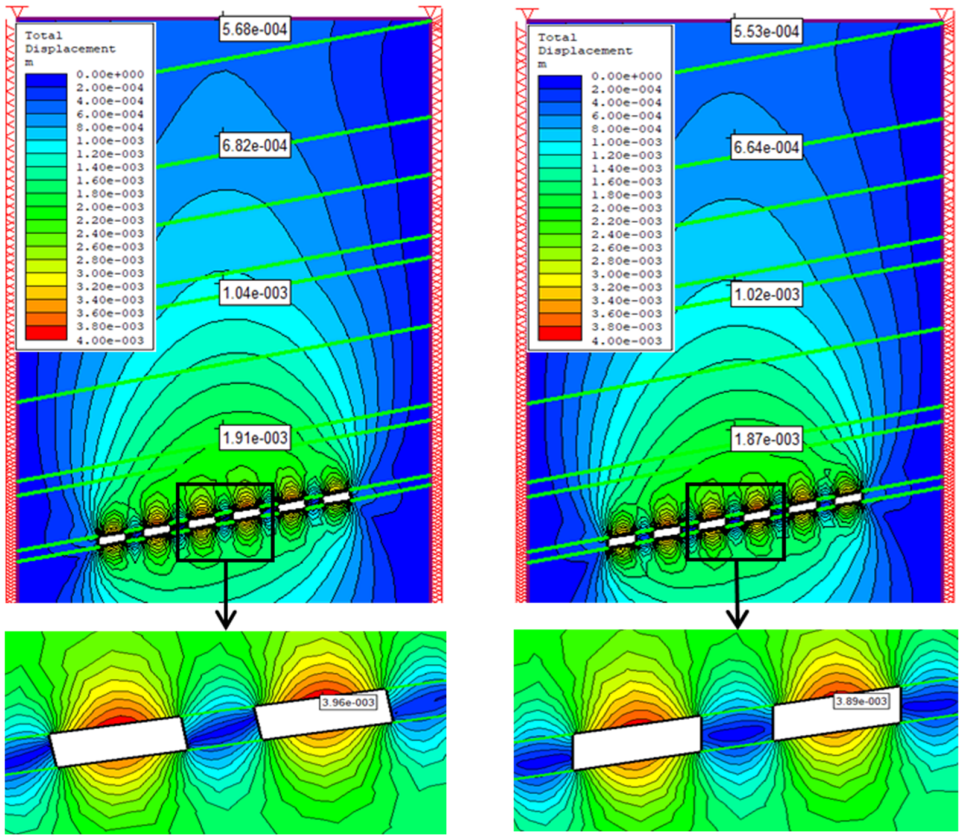

(a) (b)

Figure 13. Total displacement contours for both pillar configurations: (a) inclined A-pillars; (b) inclined B-pillars

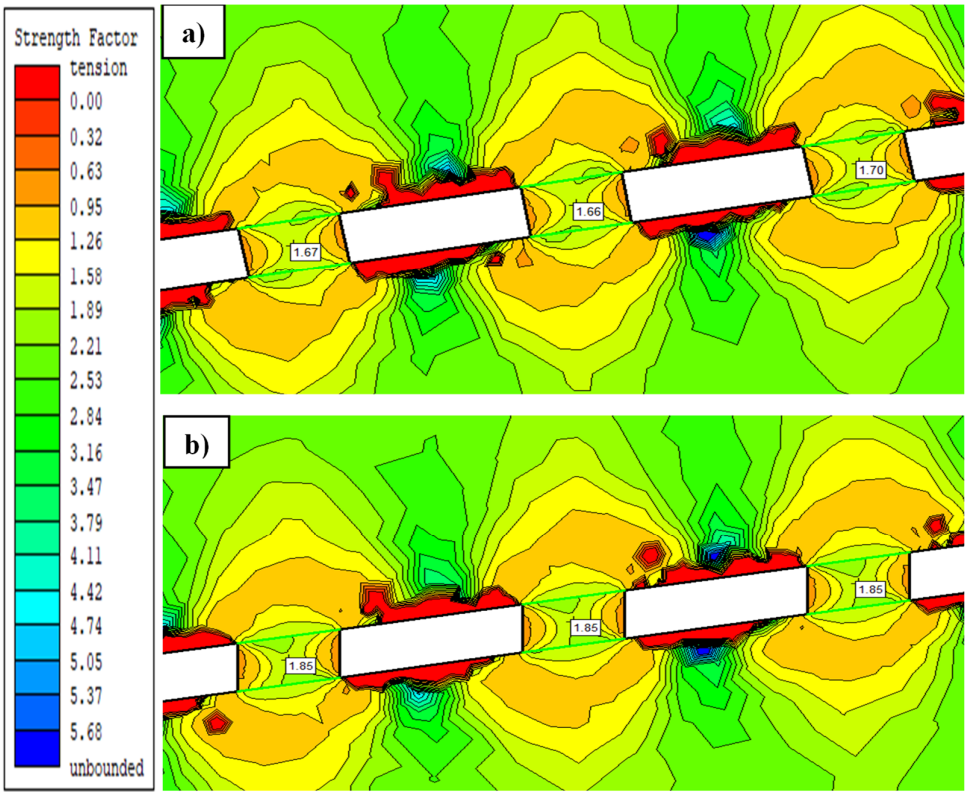

Figure 14. Strength factor contours: (a) inclined A-pillars; (b) inclined B-pillars

5. Conclusions

This study presents the geomechanical characterization of rock masses followed by analytical and numerical analyses of underground pillars subjected to combined compression and shear loads at the Chaabet El Hamra zinc mine. The main outcomes of the study are as follows:

- Comprehensive geomechanical testing and classification established reliable design parameters for the mine's rock mass.

- The integration of empirical, analytical, and numerical approaches in underground hard rock pillar design proved crucial for ensuring the safety, stability, and economic viability of mining operations.

- The analytical shear strength model indicates that the design, which incorporates 10° inclined pillars with walls perpendicular to the orebody dip, with pillars 5 m wide and 3 m high within 9 m wide rooms, achieves an extraction rate of 87.24% and a safety factor of 1.63, demonstrating a stable and secure mining operation with efficient ore recovery.

- Numerical modeling validated the reliability of the analytical model, showing a maximum displacement of 3.96 mm, negligible surface subsidence (0.57 mm), and a safety factor of 1.66, confirming structural stability.

- The selection of appropriate empirical formulas for estimating the strength of vertical pillars was critical for obtaining reliable results. Compared to other empirical formulas, the Lunder and Pakalnis formula used in this study provided more conservative analytical calculations.

- The close alignment between normal and shear stress results calculated using tributary area theory and numerical method validates both approaches for assessing pillar stability in inclined orebodies. This insight is crucial for ensuring safe mining practices and optimizing pillar design.

- Comparing pillar orientations while maintaining identical pillar and room dimensions and cover depth revealed that vertical-walled pillars (B-pillars) demonstrated superior performance over perpendicular-walled pillars (A-pillars). B-pillars provided more uniform and symmetrical stress distribution, increasing confinement at the pillar core and improving the safety factor to 1.85. These results underscore the significance of pillar geometry in room-and-pillar design for enhancing safety and long-term stability.

References

[1]. Dzimunya, N. Z., & Fujii, Y. (2024). A proposed framework to estimate pillar strength in room-and-pillar hard rock mines. In *ARMA US Rock Mechanics/Geomechanics Symposium* (p. D022S018R004). ARMA.

[2]. Toderas, M. (2024). Stability analysis of the exploitation system with room and pillar by analytical methods. *Applied Sciences*, *14*(5), 1827.

[3]. Cano Nunez, A. E., Arroyo Ortiz, C. E., & Margarida da Silva, J. (2022). Effect of Dynamic Stress Produced by Rock Blasting on the Optimal Dimensioning of Room and Pillars in Horizontal Layers. *Advances in Materials Science and Engineering*, *2022*(1), 7826557.

[4]. Pariseau, W.G. (2011). Design Analysis in Rock Mechanics, 2nd ed.; CRC Press: Boca Raton, FL, USA.

[5]. Luo, B., Ye, Y., Li, Y., Luo, J., Chen, H. (2018). Safety factor method for stability of inclined pillars under Mohr-Coulomb criterion. J. China Coal Soc, 43, 2408–2415. (in Chinese).

[6]. Cai, Y., Jin, Y., Wang, Z., Chen, T., Wang, Y., Kong, W., ... & Hu, H. (2023). A review of monitoring, calculation, and simulation methods for ground subsidence induced by coal mining. *International journal of coal science & technology*, *10*(1), 32.

[7]. Kvapil, R.L., Beaza, J.R., Flores, G. (1989). Block caving at EI Teniente Mine, Chile. Trans. Inst. Min. Metall. Sect. A Min. Technol, 98, 43–56.

[8]. Ardehjani, E. A., Ataei, M., Sereshki, F., Mirzaghorbanali, A., & Aziz, N. (2024). Examining the Impact of Coal Gas Emissions on the Stability Analysis of Coal Pillars: A Critical Literature Review. *Rudarsko-geološko-naftni zbornik*, *39*(3), 77-94.

[9]. Ardehjani, E. A., Ataei, M., Sereshki, F., Mirzaghorbanali, A., & Aziz, N. (2025). Impact of CO2 and methane adsorption and emission on coal's mechanical properties and pillar stability: Implications for ECBM and CO2 sequestration. *Energy*, *333*, 137438.

[10]. Sarfarazi, V., Haeri, H., & Khaloo, A. (2016). The effect of non-persistent joints on sliding direction of rock slopes. *Comput. Concrete*, *17*(6), 723-737.

[11]. Fu, J., Sarfarazi, V., Haeri, H., Zarei, A. S., Bahrami, R., Imani, M., & Marji, M. F. (2024). Experimental and Numerical Analyses of Shear Failure Mechanisms of Rock Bolt Surrounded by Bedded Rock. *International Journal of Geomechanics*, *24*(12), 04024276.

[12]. Hedley, D. G. F., & Grant, F. (1972). Stope-and-pillar design for the Elliot Lake Uranium Mines.

[13]. Krauland, N., & Soder, P. E. (1987). Determining pillar strength-from pillar failure observation. *E&MJ-Engineering and Mining Journal*, *188*(8), 34-40.

[14]. Lunder, P. J., & Pakalnis, R. C. (1997). Determination of the strength of hard-rock mine pillars. *CIM bulletin*, *90*(1013), 51-55.

[15]. Ghasemi, E., Ataei, M., & Shahriar, K. (2014). An intelligent approach to predict pillar sizing in designing room and pillar coal mines. International Journal of Rock Mechanics and Mining Sciences, 65, 86-95.

[16]. Ghasemi, E., Ataei, M., & Shahriar, K. (2014). Prediction of global stability in room and pillar coal mines. *Natural hazards*, *72*(2), 405-422.

[17]. Kunkyin-Saadaari, F., Offei, J. B., Sadique, S. I., Agadzie, V. K., & Forson, I. A. (2025). Investigating the Applicability of Stacked Generalization Technique for the Prediction of Hard Rock Pillar Stability Status. *Journal of Mining and Environment*, *16*(3), 907-923.

[18]. Abdollahi, M. S., Najafi, M., Yarahamdi Bafghi, A., & Rafiee, R. (2024). A new method for stability analysis of chain pillar in longwall mining by using coulmann graphical method. *Journal of Mining and Environment*, *15*(4), 1461-1476.

[19]. Najafi, M., Jalali, S. M., Sereshki, F., & Yarahmadi, B. A. (2016). Probabilistic analysis of stability of chain pillars in Tabas coal mine in Iran using Monte Carlo simulation.

[20]. Rezaei, A., Sarfarazi, V., Babanouri, N., Omidi Manesh, M., & Jahanmiri, S. (2023). Failure Mechanism of Rock Pillar Containing Two Edge Notches: Experimental Test and Numerical Simulation. *Journal of Mining and Environment*, *14*(3), 961-971.

[21]. Sarfarazi, V., Karimi Javid, H., & Asgari, K. (2021). Study of rock pillar failure consisting of non-persistent joint using experimental test and fracture analysis code in two dimensions. *Journal of Mining and Environment*, *12*(1), 163-179.

[22]. Sarfarazi, V., Fu, J., Haeri, H., Abharian, S., Rasekh, H., Behzadinasab, M., & Fatehi Marji, M. (2024). Mechanical characteristics and crack propagation mechanism in rectangular and trapezoidal specimens of excavated pillars with various cavities: experimental and numerical investigations. *Computational Particle Mechanics*, *11*(5), 2069-2087.

[23]. Fu, J., Haeri, H., Sarfarazi, V., Babanouri, N., Rezaei, A., Manesh, M. O., ... & Fatehi Marji, M. (2023). Effects of axial loading width and immediate roof thickness on the failure mechanism of a notched roof in room and pillar mining: Experimental test and numerical simulation. *Rock Mechanics and Rock Engineering*, *56*(1), 719-745.

[24]. Jessu, K. V., Spearing, A. J., & Sharifzadeh, M. (2018). Laboratory and numerical investigation on strength performance of inclined pillars. *Energies*, *11*(11), 3229.

[25]. He, Q., Li, Y., & She, S. (2019). Mechanical properties of basalt specimens under combined compression and shear loading at low strain rates. *Rock Mechanics and Rock Engineering*, *52*(10), 4101-4112.

[26]. He, Q., Li, Y., Xu, J., & Zhang, C. (2020). Prediction of mechanical properties of igneous rocks under combined compression and shear loading through statistical analysis. *Rock Mechanics and Rock Engineering*, *53*(2), 841-859.

[27]. Xu, S., Huang, J., Wang, P., Zhang, C., Zhou, L., & Hu, S. (2015). Investigation of rock material under combined compression and shear dynamic loading: an experimental technique. International Journal of Impact Engineering, 86, 206-222.

[28]. Jessu, K. V., & Spearing, A. J. S. (2018). Effect of dip on pillar strength. *Journal of the Southern African Institute of Mining and Metallurgy*, *118*(7), 765-776.

[29]. Lorig, L. J., & Cabrera, A. (2013). Pillar strength estimates for foliated and inclined pillars in schistose material. In Proceedings of the 3rd international FLAC/DEM symposium, Hangzhou, China (pp. 22-24).

[30]. Ma, T., Wang, L., Suorineni, F. T., & Tang, C. (2016). Numerical analysis on failure modes and mechanisms of mine pillars under shear loading. *Shock and Vibration*, *2016*(1), 6195482.

[31]. Garza-Cruz, T., Pierce, M., & Board, M. (2019). Effect of shear stresses on pillar stability: a back analysis of the troy mine experience to predict pillar performance at Montanore Mine. *Rock Mechanics and Rock Engineering*, *52*(12), 4979-4996.

[32]. Suorineni, F. T., Mgumbwa, J. J., Kaiser, P. K., & Thibodeau, D. (2014). Mining of orebodies under shear loading Part 2–failure modes and mechanisms. *Mining Technology*, *123*(4), 240-249.

[33]. Rashed, G., Slaker, B., Sears, M. M., & Murphy, M. M. (2021). A parametric study for the effect of dip on stone mine pillar stability using a simplified model geometry. *Mining, Metallurgy & Exploration*, *38*(2), 967-977.

[34]. Das, A. J., Mandal, P. K., Bhattacharjee, R., Tiwari, S., Kushwaha, A., & Roy, L. B. (2017). Evaluation of stability of underground workings for exploitation of an inclined coal seam by the ubiquitous joint model. International Journal of Rock Mechanics and Mining Sciences, 93, 101-114.

[35]. Das, A. J., Mandal, P. K., Paul, P. S., Sinha, R. K., & Tewari, S. (2019). Assessment of the strength of inclined coal pillars through numerical modelling based on the ubiquitous joint model. *Rock Mechanics and Rock Engineering*, *52*(10), 3691-3717.

[36]. Das, A. J., Mandal, P. K., Paul, P. S., & Sinha, R. K. (2019). Generalised analytical models for the strength of the inclined as well as the flat coal pillars using rock mass failure criterion. *Rock Mechanics and Rock Engineering*, *52*(10), 3921-3946.

[37]. Sun, L., Ye, Y., Luo, B., Hu, N., & Li, P. (2021). Theoretical Analysis for Stability Evaluation of Rock Mass Engineering Structure under Combined Compression-Shear Loading: A Case Study of Inclined Pillar. *Applied Sciences*, *11*(23), 11439.

[38]. ENOF, (2024). Geological report of the Chaabet El Hamra zinc deposit, Algiers.

[39]. AFNOR, (2000). NF P94-420. Determination of uniaxial compressive strength. Association Française de Normalisation

[40]. AFNOR, (1993). NF P94-064. Soils: investigation and testing. Density of a dehydrated rock sample. Hydrostatic weighing method. Association Française de Normalisation

[41]. Mouerri, A., Hadji, R., Zahri, F., Hamed, Y., & Serhane, B. (2024). Multidisciplinary evaluation of geological, geotechnical, geomechanical, and hydrogeological parameters for assessing slope stability in the Aures Mountain Quarry. *Geomatics, Landmanagement and Landscape*.

[42]. Bieniawski, Z. T. (1989). *Engineering rock mass classifications: a complete manual for engineers and geologists in mining, civil, and petroleum engineering*. John Wiley & Sons.

[43]. Hoek, E., & Marinos, P. (2000). Predicting tunnel squeezing problems in weak heterogeneous rock masses. *Tunnels and tunnelling international*, *32*(11), 45-51.

[44]. Hoek, E., Carranza-Torres, C., & Corkum, B. (2002). Hoek-Brown failure criterion-2002 edition. *Proceedings of NARMS-Tac*, *1*(1), 267-273.

[45]. Aydan, Ö., Akagi, T., & Kawamoto, T. (1996). The squeezing potential of rock around tunnels: theory and prediction with examples taken from Japan. *Rock mechanics and rock engineering*, *29*, 125-143.

[46]. Pariseau, W. G. (1982). Shear stability of mine pillars in dipping seams. In *ARMA US Rock Mechanics/Geomechanics Symposium* (pp. ARMA-82). ARMA.

[47]. Kumar, R., Mandal, P. K., Ghosh, N., Das, A. J., & Banerjee, G. (2023). Design of stable parallelepiped coal pillars considering geotechnical uncertainties. *Rock Mechanics and Rock Engineering*, *56*(9), 6581-6602.

[48]. Giafferi, J. L. (2003). Characterisation of rock masses useful for the design and the construction of underground structures. *AFTES guidelines; Tunnels et Ouvrages souterrains*, (177), 2-49.

[49]. Woessner, W. W., & Poeter, E. P. (2020). *Hydrogeologic properties of earth materials and principles of groundwater flow*. Groundwater Project.

[50]. Schöpfer, M. P., Abe, S., Childs, C., & Walsh, J. J. (2009). The impact of porosity and crack density on the elasticity, strength and friction of cohesive granular materials: Insights from DEM modelling. *International journal of rock mechanics and mining sciences*, *46*(2), 250-261.

[51]. Radouane, N., Boukelloul, M., & Fredj, M. (2015). Stability analysis of underground mining and their application on the Mine Chaabte El Hamra, Algeria. *Procedia Earth and Planetary Science*, *15*, 237-243.

[52]. Monsalve Valencia, J. J. (2022). A Risk-Based Pillar Design Approach for Improving Safety in Underground Stone Mines. PhD Dissertation, Virginia Pollytechnic Institute and State University. Blacksburg, Virginia.

نشریه مهندسی معدن و محیط زیست
نشانی نشریه: www.jme.shahroodut.ac.ir
انجمن مهندسی معدن ایران
دانشگاه صنعتی شاهرود

تحلیل تحلیلی و عددی پایداری ستون‌های زیرزمینی تحت بارگذاری برشی: مطالعه موردی معدن روی چابت الحمرا، الجزایر

سامیا چاوی[۱]، عادل جلالی[۱*]، زید بنغازی[۱] و دیبوجیت سارکر[۲]

۱ .آزمایشگاه محیط زیست، گروه معدن و ژئوتکنولوژی، موسسه معدن، دانشگاه شیخ شیخ العربی تبسی، تبسا، الجزایر
۲. HNTB، جاده انتین ۹، پارسیپانی، نیوجرسی ۰۷۰۵۴، ایالات متحده آمریکا

اطلاعات مقاله

تاریخ ارسال: ۲۰۲۵/۰۸/۱۶
تاریخ داوری: ۲۰۲۵/۰۹/۲۵
تاریخ پذیرش: ۲۰۲۵/۱۱/۰۲

DOI:10.22044/jme.2025.16677.3272

کلمات کلیدی

نرخ استخراج
ستون‌های شیب‌دار
ضریب اطمینان
مدل تحلیلی
مدل‌سازی عددی

چکیده

هدف این مطالعه بررسی پایداری اتاق‌ها و ستون‌ها در امتداد توده معدنی شیب‌دار روی در معدن زیرزمینی Chaabet El Hamra (Setif، الجزایر) است. پایداری در ابتدا با استفاده از یک مدل تحلیلی مقاومت برشی ارزیابی شد و نتایج متعاقباً از طریق مدل‌سازی عددی اعتبارسنجی شدند. مشخصه‌یابی ژئومکانیکی، تخلخل بینابینی کم، مقاومت فشاری تک‌محوری قوی تا بسیار قوی از ۵۰.۴ مگاپاسکال تا ۱۲۹ مگاپاسکال و تخلخل ثانویه قابل توجه مرتبط با شکستگی را نشان داد. مقادیر رتبه‌بندی توده سنگ (RMR89) و شاخص مقاومت زمین‌شناسی (GSI) کیفیت سنگ را متوسط تا خوب نشان می‌دهند. طراحی معدن شامل ستون‌های مربعی با شیب ۱۰ درجه و دیوارهایی است که در ابتدا عمود بر شیب توده معدنی قرار گرفته‌اند و ۵ متر عرض و ۳ متر ارتفاع دارند. اتاق‌ها که در زیر عمق پوشش ۱۴۵.۳ متر قرار دارند، ۹ متر عرض دارند. این پیکربندی نرخ استخراج مؤثر ۸۷.۲۴٪ و ضریب ایمنی ۱.۶۳ را به همراه داشت که نشان دهنده شرایط پایدار معدنکاری است. شبیه‌سازی المان محدود فاز دوبعدی این یافته‌ها را تأیید کرد و حداکثر جابجایی ۳.۹۶ میلی‌متر، نشست سطح ۰.۵۷ میلی‌متر و ضریب ایمنی ۱.۶۶ را نشان داد که نشان‌دهنده حداقل تأثیر زیست‌محیطی و پایداری بلندمدت است. نتایج تنش برشی/فشاری حاصل از نظریه ناحیه شاخه فرعی، با نتایج عددی همسو شده و هر دو رویکرد را برای توده‌های معدنی شیب‌دار تأیید می‌کند. در نهایت، دیواره‌های ستون، که در ابتدا عمود بر شیب توده معدنی بودند، نسبت به صفحه افقی به صورت عمودی اصلاح شدند، در حالی که همان ابعاد ستون و اتاق و عمق پوشش را حفظ می‌کردند. این تنظیم با افزایش توزیع تنش و محصورشدگی هسته ستون، پایداری را بهبود بخشید و ضریب ایمنی را به ۱.۸۵ افزایش داد.

نویسنده مسئول مکاتبات: i.gholamnejad@yazd.ac.ir (ع. جلالی)